Weibull strength size effect of diamond wire sawn photovoltaic silicon wafers

Louise Carton, Roland Riva, Daniel Nélias, Marion Fourmeau

Weibull strength size effect of diamond wire sawn photovoltaic silicon wafers

Louise Carton [1,2,3], Roland Riva [1], Daniel Nélias [3], Marion Fourmeau [3]

[1] *Univ Grenoble Alpes, CEA-LITEN, INES, 50 avenue du Lac Léman, F-73375 Le Bourget-du-Lac, France*

[2] *Agence de l'environnement et de la Maîtrise de l'Energie 20 avenue du Grésillé - BP 90406 49004 Angers Cedex 01 France*

[3] *Univ Lyon, INSA-Lyon, CNRS UMR5259, LaMCoS, F-69621, France*

Corresponding author: L. Carton - louise.carton@cea.fr

Abstract

A good comprehension of the mechanical properties of photovoltaic silicon wafers is crucial to maintain low breakage rates during solar cell manufacturing. As brittle material, silicon wafers are theoretically subject to a strength size effect. This study aims at determining whether this effect should be considered when comparing the strength of photovoltaic wafers. We derive a theoretical strength scaling law and perform an extensive experimental study on 240 diamond-wire sawn silicon wafers, which have the particularity of exhibiting an anisotropy in Weibull parameters. We compare test results from three different bending configurations and show that a size effect is only observable when loading the wafers perpendicular to the saw marks. Strength values obtained when loading the wafers in the direction of the wire yield identical results regardless of the size of the tested area. These findings can open up prospects for the standardization of testing methods for photovoltaic wafers.

Keywords

- Silicon wafer
- Diamond wire sawing
- Four-line bending
- Weibull distribution
- Strength size effect

Acknowledgments

This work was supported by the French Environment and Energy Management Agency (ADEME), which is gratefully acknowledged.

1 Introduction

Crystalline silicon-wafer based technology accounts for more than 90% of the production of photovoltaic (PV) solar cells [1]. With the advantages such as lower silicon material loss, higher process productivity and easier recycling, diamond wire sawing technology (DWS) has replaced the historical slurry sawing technology to process PV silicon wafers [2,3]. The wafering process remains a major cost driver for the PV industry, as it accounts for 52% of the module price [1]. In particular, the need to lower the silicon material waste implies sawing wafers that are both thinner and larger, which can lead to significantly higher breakage rates during the processing steps. Studying the mechanical strength of PV silicon wafers has therefore always been an important subject, with a recent focus on the influence of the DWS process [4,5].

Of the various methods available to characterize brittle thin specimens such as silicon wafers, the four-line bending setup remains the most commonly used in literature, as it provides a constant stress distribution over a large area. Single crystalline silicon has a measured fracture toughness ranging between 1 and 2 $MPa.m^{1/2}$ depending on crystallographic orientation [6] and can as such be considered a technical ceramic. Following this reasoning, several studies chose to design their four-line bending setup according to the guidelines of ASTM C1161 [7–10]. However, the recommendations are often not suited to the geometry of photovoltaic silicon wafers, in particular because of their high length-to-thickness ratio. The maximum plate deflection can reach several times the thickness value, thus making the use of the standard beam formula to evaluate wafer strength highly questionable. Working with rectangular samples of smaller dimensions is an option to minimize this effect, but it requires an extra dicing step [11–13]. An alternative method consists in knowingly choosing setup dimensions that do not respect the standard ASTM C1161, and to use a finite element model to evaluate stress at the time of failure [14]. To overcome this global issue, a standard test method for strength testing of photovoltaic wafers was recently developed [15]. It provides requirements to design a four-line bending setup suited for full-size silicon wafers and lookup tables to compute fracture stresses. However, given the recentness of this contribution, there are yet only very few studies relying on it [16].

Regardless of the test or sample dimensions chosen, nearly all studies agree that the large scattering of failure stress values obtained when testing silicon wafers requires statistical treatment. Because of its ability to evaluate both the level and scattering of strength values, Weibull probability function [17] is the most widely used to describe fracture behavior of PV silicon wafers. It is worth noting that Weibull theory for silicon wafers is usually used in its simplest form and without questioning its validity or limits. In particular, with a very few rare exceptions [18], the possible influence of a strength size effect is never considered, although it is known to be a major concern in the field of technical ceramics [19,20]. This omission is usually justified by the fact that each study uses a given sample geometry (typically a 156 x 156 mm wafer of thickness 180 µm) and identical test dimensions, so that the effective volume can be considered similar. While this holds true when comparing the results within each study, the literature review presented in the previous paragraph showed that there exists a large variety of setup and wafer dimensions (square or rectangular, 156 mm or 125 mm long). It is then legitimate to question whether the strength results obtained from different studies can be directly compared.

The present study therefore aims at determining if silicon wafers do present a significant size effect and how it should be taken into account when comparing strength results from different studies. The investigation focuses here on diamond wire sawn monocrystalline silicon wafers, which are an ideal case study to evaluate the influence of the strength size effect. Indeed, DWS wafers are known to have an anisotropy in strength properties depending on whether the stress is applied parallel or perpendicular to saw marks left by the diamond wire [21,22]. Thus, while usually the influence of Weibull parameters on the size effect has to be studied numerically, typically via the use of Monte Carlo simulations [23,24], DWS wafers offer the possibility to experimentally verify the contribution of the size effect with changing Weibull parameters.

2 Applying Weibull size effect theory to silicon wafers

Breakage stress values obtained for silicon wafers that are deemed identical will exhibit large scattering. This dispersion results from the brittle nature of silicon: the strength of a silicon wafer is ultimately controlled by the density, size and geometry of its defects, which can vary strongly even within a single series. These characteristics are random variables, and the failure stress of the wafer under a given applied load becomes a statistical variable. Failure is then a random event with a certain probability or likelihood of coming true under given circumstances. The mean stress value is therefore not sufficient to represent the strength of a set of wafers and the values require statistical treatment.

There exist different statistical approaches to model brittle failure, which all aim at linking the characteristics of the defect population and the characteristics of the stress field to the material failure probability. As thoroughly detailed in the review from Danzer [25], these approaches are based on two main assumptions: (i) failure of brittle materials initiates at flaws (described as cracks) which are randomly distributed in the sample and (ii) if one crack becomes critical, failure of the specimen occurs. The second assumption is best known as the weakest link hypothesis, i.e. the survival probability of a specimen is the product of survival probabilities of each volume element within the specimen [26]. The mechanical strength of the entire specimen is therefore defined by its weakest defect. For a given volume, a sample with more defects is more likely to fail than a sample with less defects. Conversely, a sample of greater volume has a greater chance of having a critical defect than a smaller sample. This phenomenon is known as the *size effect*.

From the two previous assumptions, we can obtain the most general expression for the probability of failure of a specimen [27]:

$$P(\sigma, V) = 1 - \exp[-N_c(\sigma, S)] \tag{1}$$

where $N_c(\sigma, S)$ is the mean number of critical flaws per specimen, which depends on the size and geometry of the specimen S and on the geometry and level of the stress field σ.

Weibull's statistical theory of fracture [17,28], which was first introduced in 1939, can be considered as a special solution of equation (1). Weibull indeed showed that a wide variety of problems can be described if the critical flaw population follows an inverse power law:

$$N_c(\sigma, V) = -\frac{V}{V_0}\left(\frac{\sigma - \sigma_u}{\sigma_0}\right)^m \tag{2}$$

where m is the Weibull modulus (shape parameter), σ_0 is the characteristic strength value (scale parameter), and σ_u the threshold stress below which the specimen will not fail (location parameter). The last three parameters are associated with the material and are independent of size. V_0 is the chosen normalizing volume, which allows to adjust the dimension of the shape parameter. For a uniaxial homogeneous tensile stress state, Weibull therefore expresses the failure probability P of a specimen of volume V subjected to a uniaxial tensile stress σ as:

$$P(\sigma, V) = 1 - \exp\left(-\frac{V}{V_0}\left(\frac{\sigma - \sigma_u}{\sigma_0}\right)^m\right) \tag{3}$$

This famous strength distribution function is the most widely used to described fracture behavior of silicon wafers. In the specific case of wafers for PV applications, Weibull's model is, to the best of our knowledge, the only implemented model. In most cases, for the sake of simplicity the threshold stress is assumed to be zero, and the Weibull distribution can be reduced to a simplified two-parameter form:

$$P(\sigma, V) = 1 - \exp\left(-\frac{V}{V_0}\left(\frac{\sigma}{\sigma_0}\right)^m\right) \tag{4}$$

This simplification allows to obtain a conservative prediction, and the remaining two parameters are much simpler to estimate [29]. Several studies discussed the effect of assuming $\sigma_u = 0$ on the estimation of the Weibull parameters [30,31]. Lu et al. [30] proposed a simple quantitative procedure to highlight the effects of the threshold stress, and concluded that a compromise should be made between simplicity of the two-parameter Weibull distribution and applicability of the three-parameter Weibull distribution as the threshold stress of the considered samples increases. Malzbender et al. [32] demonstrated that the three-parameter Weibull statistics is more appropriate for fracture characterization of thin ceramic components, but their observations were based on one experimental sample and it is not straightforward to extend their conclusions to other types of materials. More recently, Deng et al. [31] conducted an extensive examination based on Monte-Carlo simulation and showed that the two-parameter Weibull function is sufficiently suitable for the description of the statistical variation of the measured strength sample, regardless of whether the strength follows a two-parameter or a three-parameter Weibull distribution. Since values of Weibull parameters obtained for diamond-wire sawn silicon wafers are within the examined range used in their simulations, we chose to rely on their conclusions and use a two-parameter Weibull distribution.

It should be noted that this choice is made by almost all studies focusing on the strength distribution of silicon wafers. A notable exception can be found in the work of Saleh et al. [33], who used a three-parameter function to describe the size effect in polycrystalline silicon wafers. However, their investigations were performed on micro machined samples with extremely high strength values (in the order of 2-5 GPa), thus justifying the use of a threshold stress value, while failure stresses of DWS silicon wafers rarely exceed a few hundreds of MPa.

In the case where a non-uniform stress state is applied on the specimen, each volume element has a different failure probability. The formulation of equation (4) becomes an integral over the entire specimen volume, which makes sense for a bending test:

$$P(\sigma, V) = 1 - \exp\left[-\frac{1}{V_0}\int_V \left(\frac{\sigma(x,y,z)}{\sigma_0}\right)^m dV\right] \tag{5}$$

Introducing the maximum stress σ_{max} and rearranging the terms of equation (5) yields:

$$P(\sigma, V) = 1 - \exp\left[-\frac{1}{V_0}\left(\frac{\sigma_{max}}{\sigma_0}\right)^m \int_V \left(\frac{\sigma(x,y,z)}{\sigma_{max}}\right)^m dV\right] \tag{6}$$

The formulation of equation (6) enables to reveal the effective volume parameter $\boldsymbol{V_{\text{eff}}}$, which is defined as the integral over the specimen volume of the ratio between the local stress value $\sigma(x,y,z)$ and the maximum stress value σ_{max} :

$$V_{\text{eff}} = \int_V \left(\frac{\sigma(x,y,z)}{\sigma_{max}}\right)^m dV \tag{7}$$

The effective volume can be interpreted as the size of an equivalent uniaxial tensile specimen that has the same failure probability as the specimen subjected to a non-uniform stress state. It accounts for the specimen geometry and the stress gradient and can be used to compare the failure probabilities of specimens of different sizes and subjected to different stress fields. Let indeed two samples consisting of the same material and of different effective volumes such that $V_{\text{eff},1} > V_{\text{eff},2}$. The ratio of the stresses to apply on each of the samples for them to have the same failure probability P can be expressed by combining the two failure probabilities:

$$P(\sigma_1, V_{\text{eff},1}) = 1 - exp\left[-\frac{V_{\text{eff},1}}{V_0}\left(\frac{\sigma_1}{\sigma_0}\right)^m\right] \text{ and } P(\sigma_2, V_{\text{eff},2}) = 1 - exp\left[-\frac{V_{\text{eff},2}}{V_0}\left(\frac{\sigma_2}{\sigma_0}\right)^m\right] \tag{8}$$

$$\frac{\sigma_2}{\sigma_1} = \left(\frac{V_{\text{eff},1}}{V_{\text{eff},2}}\right)^{\frac{1}{m}} \tag{9}$$

With a positive Weibull modulus and $V_{\text{eff},1} > V_{\text{eff},2}$, equation (9) leads to $\sigma_1 < \sigma_2$, i.e. the specimen with smaller effective volume has a higher mechanical strength. It is worth noting that $\boldsymbol{V}_{\text{eff}}$ depends on the Weibull modulus of the sample considered. Specifically, the size effect increases with decreasing Weibull modulus, as demonstrated by equation (9). This means that materials with high defect dispersion are more sensitive to the size effect.

The previous approach is based on the assumption that the critical defects are located in the volume of the material considered. However, if failure initiates mainly from surface micro-defects, it is more relevant to consider the effective surface $\boldsymbol{S}_{\text{eff}}$ [34,35]. The integration in equation (7) is then performed over the sample surface instead of the volume and the previously three-dimensional stress function $\sigma(x, y, z)$ becomes two-dimensional. Fischer [35] alternatively proposed an effective shell model $\boldsymbol{SH}_{\text{eff}}$, which is derived under the assumption that the critical defects are located in a thin shell layer. The thickness of the layer δ is determined by minimizing the scatter in strength values obtained experimentally. All models are valid and are usually chosen according to the specific defect population in order to improve the reliability of experimental results.

The identification of a specific defect population responsible for silicon wafer failure is not straightforward. While it is generally accepted that the most critical damage regarding wafer fracture strength is created during the sawing process, the nature of this damage is however complex and multiple. In diamond-wire sawing, material removal occurs via the combined scratching and indenting actions of the diamond particles on the silicon surface, thus generating long parallel grooves oriented in the direction of the wire, as well as randomly distributed indentation pits [36,37]. These features can be considered as *surface defects (*Fig. 1.a). But the abrasion mechanism also damages the wafer deeper under the surface, through the formation of microcracks with length varying from a few tenths up to several tens of microns [38–40] depending on the sawing parameters (Fig. 1.b). These microcracks are then designated as *subsurface defects*. Finally, the slicing process can also induce some micrometer scale chipping at the wafer sides [5], thus creating *edge defects* (Fig. 1.c).

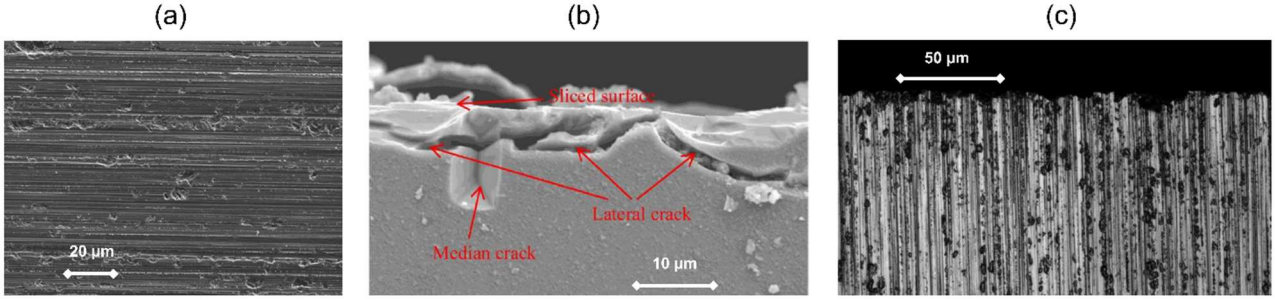

Fig. 1 Examples of silicon wafer characteristic defects (a) Indentation pits at the wafer surface [36] (b) Microcracks at the wafer subsurface [38] (c) Chipping defects at the wafer edges

It has furthermore never been proven that initial *bulk defects* play no role in the mechanical properties of silicon wafers. On the contrary, some studies have even shown that intrinsic factors such as non-uniform residual stress caused by solidification [41] or bulk defects in the form of dislocations or inclusions [42,43] can influence the mechanical strength of wafers after the sawing process.

Although many types of defect population co-exist in a silicon wafer, one could theoretically identify the critical flaw size using the Griffith criterion, i.e. brittle failure occurs if the stress intensity factor K of the critical flaw exceeds the fracture toughness K_C. The most general expression for the stress intensity factor is given by [44]:

$$K = \sigma Y \sqrt{\pi a} \tag{10}$$

where σ is the nominal stress in the specimen, a is the crack length and Y is a dimensionless geometric factor. From equation (10), we can defined the critical Griffith crack length, i.e. the crack length for which the stress intensity factor is higher than the fracture toughness ($K \geq K_C$):

$$a_c = \frac{1}{\pi} \cdot \left(\frac{K_c}{Y\sigma}\right)^2 \tag{11}$$

For a very small penny shaped volume crack, Y is $2/\pi$ [45]. If we consider the fracture strength of a silicon wafer to be σ = 250 MPa (this value is based on previous findings from the authors [46]) and a fracture toughness K_c = 1 MPa.m$^{1/2}$, the critical radius of a volume defect is therefore a_c = 5 µm, i.e. 10 µm diameter. It is very unlikely that volume defects of such size exist in a silicon wafer, and it could therefore be reasonable to neglect the influence of volume defects.

Nevertheless, one could theoretically derive four different types of models to study the strength size effect in silicon wafers:

- A model based on an effective volume $\boldsymbol{V_{\text{eff}}}$ which would assume that the critical defects are equally distributed throughout the entire wafer volume
- A model based on an effective surface $\boldsymbol{S_{\text{eff}}}$, which would assume that the critical defects are located at the surface of the wafer
- A model based on an effective shell layer $\boldsymbol{SH_{\text{eff}}}$ which assumes the critical defects are located close under the surface in a thin layer of thickness *e*
- A model based on an effective length $\boldsymbol{L_{\text{eff}}}$ which assumes that the critical defects are located on the edges of the wafer

However, deriving these models for silicon wafers submitted to a four-line bending setup will lead to the same strength scaling law. In other words, regardless of the assumption made on defect population, the expressions for strength ratio from one flexure configuration to another will be identical. This scaling equivalence has already been highlighted by several studies over the past: Quinn showed that the ratio of strength from any two flexure configurations (three or four-point bending for example) is identical for volume or surface scaling, provided the beam geometries have constant cross-sectional size and shape [20]. More recently, Bhushan demonstrated that this independence holds for bi-modular cylindrical ceramic specimens [47].

In the following sections, we will show that the scaling equivalency also applies to the geometry of our samples, by deriving the expressions for a typical silicon photovoltaic wafer, with 156 x 156 mm square shape and thickness ranging from 100 to 200 µm, tested in a four-line bending setup. The geometry and parameters used for the equations are shown in Fig. 2.

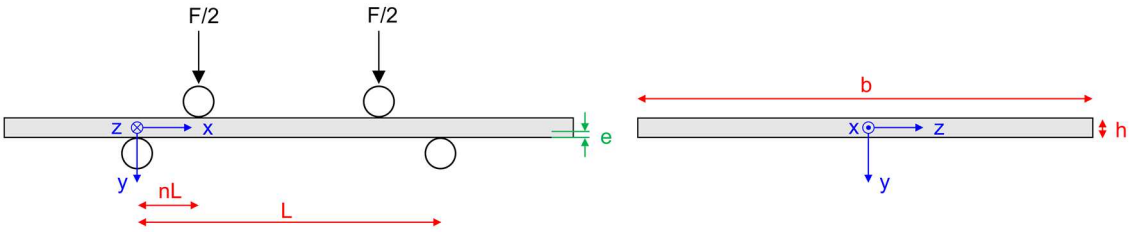

Fig. 2 Geometry and coordinate system used to derive the size effect equation

In Weibull theory, effective volumes are only determined for positive stress values. Tensile stresses are indeed more critical for brittle materials such as silicon than compressive stresses, which inhibit the phenomenon of defect propagation. In a compressive stress field, the effective volume will therefore always be zero.

In the case of a four-line bending test, the upper part of the wafer above the neutral axis is subjected to compressive stresses so the failure probability is zero. The size effect equation is therefore integrated only over the area submitted to tensile stresses, i.e. in the lower part of the samples below the neutral axis and between the lower supports.

Because the thickness of silicon wafers is extremely small compared to the side dimensions ($^{b}/_{h} \sim 10^{3}$), the area of lateral vertical surfaces of the plate (at $z = -{}^{b}/_{2}$ and $z = +{}^{b}/_{2}$) can be neglected compared to the size of the lower horizontal surface. Therefore, contrary to what is done in Fischer's work [8], the expression for the effective surface S_{eff} is only integrated from *0* to *L* along the x axis and from *0* to *b* along the z axis. The similar approximation is done for the expression of surface shell layer. The expressions and corresponding volumes, surfaces and lengths used to integrate the models are summarized in Fig. 3.

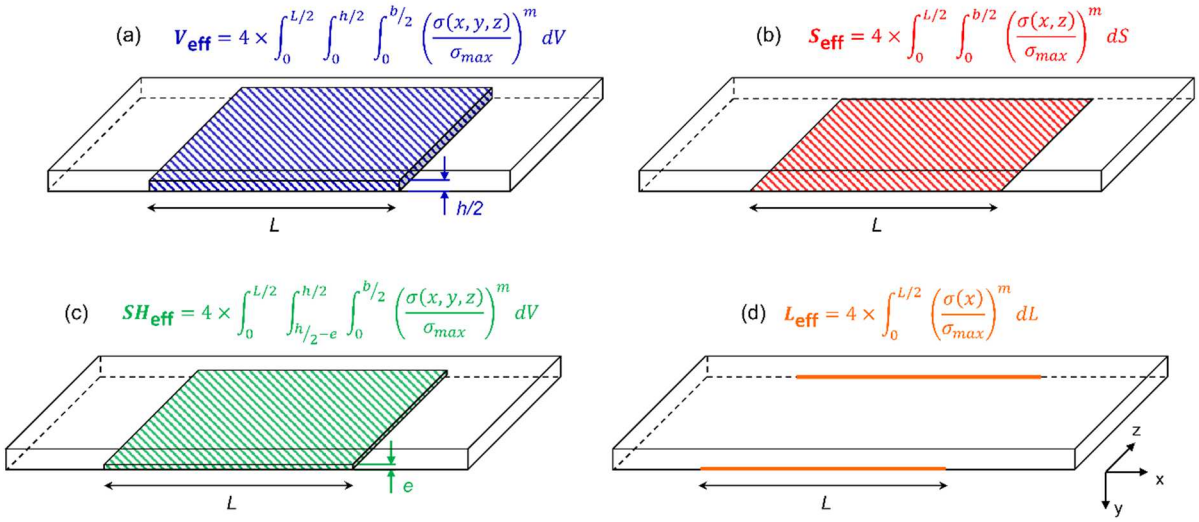

Fig. 3 Integration expressions and geometries used to derive the size effect equations of (a) the effective volume (b) the effective surface (c) the effective shell layer and (d) the effective length for a wafer tested in a four-line bending set up (the length L is the distance between the lower supports)

The development of the formulae is exemplary shown for the effective shell layer SH_{eff} in the following section. The position and orientation of the coordinate system used for the integration is as illustrated in Fig. 2. Considering the double symmetry of the setup with respect to the *(xz)* and *(yz)* planes, the expression for the effective shell layer can be written as:

$$SH_{\text{eff}} = 4 \times \int_0^{L/2} \int_{\frac{h}{2}-e}^{h/2} \int_0^{\frac{b}{2}} \left(\frac{\sigma(x,y,z)}{\sigma_{max}}\right)^m dxdydz \tag{12}$$

The stress function $\sigma(x,y,z)$ is given by:

$$\begin{cases} \sigma(x,y,z) = \dfrac{6Fxy}{bh^3} & for\ 0 < x < nL \\ \sigma(x,y,z) = \dfrac{6FnLy}{bh^3} & for\ nL < x < \dfrac{L}{2} \end{cases} \tag{13}$$

And the maximum stress σ_{max} occurs between the loading rollers and for $y = {}^{h}/_{2}$:

$$\sigma_{max} = \frac{3FnL}{bh^2} \tag{14}$$

Introducing equations (13) and (14) in the expression for the effective shell layers yields:

$$\begin{aligned} SH_{\text{eff}} &= 2b \times \left[\int_0^{nL} \int_{\frac{h}{2}-e}^{\frac{h}{2}} \left(\frac{2xy}{hnL}\right)^m dxdy + \int_{nL}^{L:2} \int_{\frac{h}{2}-e}^{\frac{h}{2}} \left(\frac{2y}{h}\right)^m dxdy \right] \\ &= Lb \times \frac{h^{m+1} - (h-2e)^{m+1}}{h^m (m+1)^2} \times (m + 1 - 2nm) \end{aligned} \tag{15}$$

The equations for the three other size effect models are derived similarly based on the expressions from Fig. 3. The corresponding expressions are given in Table 1.

Table 1 Size effect equations for the four models considered

Size effect model	Equation
Effective volume V_{eff}	$\frac{bhL}{2} \times \frac{m+1-2nm}{(m+1)^2}$
Effective surface S_{eff}	$bL \times \frac{m+1-2nm}{m+1}$
Effective shell SH_{eff}	$Lb \times \frac{h^{m+1}-(h-2e)^{m+1}}{h^m(m+1)^2} \times (m+1-2nm)$
Effective length L_{eff}	$2L \times \frac{m+1-2nm}{m+1}$

Considering two different four-line bending setups with parameters (L_1, n_1) and (L_2, n_2), the strength scaling equation (9) can be applied to the expressions in Table 1 to compare the strengths σ_1 and σ_2 measured with the two configurations. We consider here that the subsurface damage layer is the same for all samples ($e_1 = e_2$). In the special case where the cross-sectional size of the bending bars is the same, i.e. $b_1 = b_2$ and $h_1 = h_2$, the following equation holds true:

$$\frac{\sigma_2}{\sigma_1} = \left(\frac{V_{\text{eff},1}}{V_{\text{eff},2}}\right)^{\frac{1}{m}} = \left(\frac{S_{\text{eff},1}}{S_{\text{eff},2}}\right)^{\frac{1}{m}} = \left(\frac{SH_{\text{eff},1}}{SH_{\text{eff},2}}\right)^{\frac{1}{m}} = \left(\frac{L_{\text{eff},1}}{L_{\text{eff},2}}\right)^{\frac{1}{m}} = \frac{L_1}{L_2} \times \frac{m+1-2n_1m}{m+1-2n_2m} \tag{16}$$

Equation (16) confirms that all models are equivalent and that the ratio of stresses is therefore independent of the assumption made for flaw distribution. The strength size effect depends only on the four-line bending setup parameters (L, n) and the Weibull modulus m. For simplicity's sake, in the following experimental part of this work, we will therefore only consider the expression for the effective length L_{eff}.

3 Experimental approach

3.1 Samples

The wafers used for this study were obtained from a <100> oriented monocrystalline silicon ingot grown by the Czochralski process which was then shaped into a pseudo-square brick with <100> oriented sides. The brick was sawn using a wire of 80 µm core diameter with 8–16 µm diamond particles with a fixed nominal wafer thickness of 180 µm. Due to the cubic symmetric of the crystal lattice, monocrystalline silicon exhibits an anisotropic elastic behavior, which can be described by the fourth-order stiffness tensor $\boldsymbol{C}$ owning three independent parameters:

$$C_{11} = 165.7 \text{ GPa}$$

$$C_{12} = 63.9 \text{ GPa}$$

$$C_{44} = 79.6 \text{ GPa}$$

The theoretical Young's modulus of the wafers is therefore 130 GPa, which corresponds to the value along the [100] direction. A total of 240 neighboring wafers were collected directly after the sawing process. No chemical or mechanical polishing was applied to the samples. All wafers thus exhibit the characteristic saw marks caused by the back-and-forth movement of the wire (Fig. 4). The as-cut thickness and total thickness variation (TTV) of all wafers were measured using a multi-sensor capacitive system. This technology uses capacitive sensors to measure the local thickness at 45 points evenly distributed on the wafer surface. The as-cut thickness of the entire wafer is then calculated as the average of the 45 values, and the TTV as the difference between the largest and smallest values. The mean value and standard deviation are given in Table 2.

Table 2 Mean thickness and TTV of the tested series of wafers

Mean thickness ± standard deviation (µm)	Mean TTV ± standard deviation (µm)
179.0 ± 0.9	6.9 ± 2.0

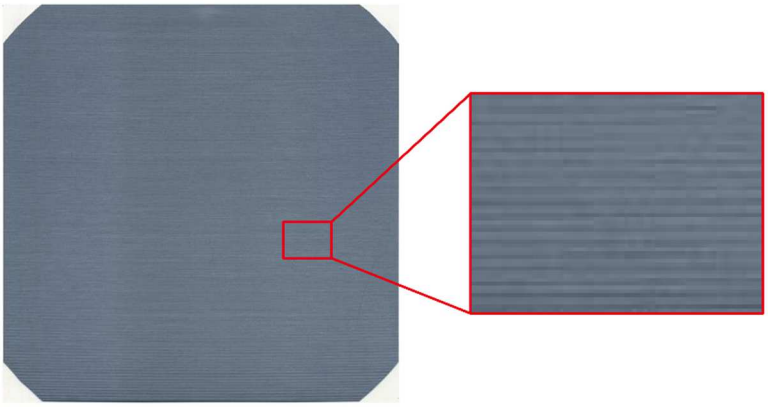

Fig. 4 Scanning image of a diamond-wire sawn as-cut monocrystalline silicon wafer

3.2 Test setup

The four-line bending setup used in this investigation is mounted on a universal testing machine (INSTRON 5965). The support and loading devices are steel cylindrical rollers with a diameter of 8 mm. The displacement of the loading rollers is imposed, and both the force F and displacement δ are recorded during the test. The distance between the rollers, which is manually adjustable, is the parameter that allows to modify the effective volumes (or surfaces and lengths) and therefore to create a strength size effect.

The adjustment of the inner and outer spans is however limited by the geometry of the wafers. Indeed, because of the aforementioned high length-to-thickness ratio (≈ 10^3), the samples are extremely flexible and the deflection values reached before failure can be very high (up to 30 mm). Now, in a four-line bending setup, the maximum stress value that can be reached during a test is limited. Indeed, as the displacement δ of the loading rollers increases, the bending radius ρ decreases until it reaches a geometrical limit. If we assume that the plate undergoes pure bending, this geometrical limit can be seen as the moment where the bending radius equals half the outer span L of the four-line bending test. Fig. 5 schematically illustrates this by showing four different bending positions corresponding to different bending radius values. The last position for which $\rho = {}^{L}/_{2}$ is the maximum bending position that the plate can reach. If further displacement is applied, the sample does not bend further, it simply slides downwards while keeping the same bending radius, and the stress remains constant.

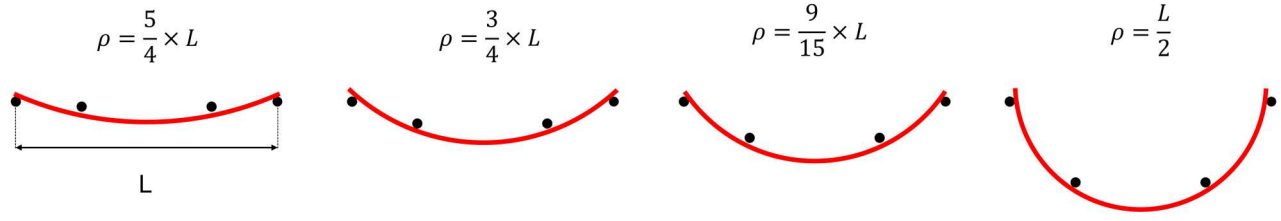

Fig. 5 Schematic illustration of the decrease of the bending radius during a four-line bending test

Reaching the maximum bending position during a test should of course be avoided, as it would mean that the maximum wafer fracture stress has not been reached and either the wafer won't break at all, or it will break when it comes into contact with the lower part of the setup. In either case, the stress results will be biased. This limitation essentially means that it is not possible to

choose an extremely large span distance for the four line bending test, because the tested specimen will very likely “fall” from the setup before it reaches failure.

With these limitations in mind and with the help of some preliminary tests, we chose three different span configurations to evaluate the size effect of the silicon wafers, thereafter referred to by their outer and inner span: 60-32 mm, 80-48 mm and 100-70 mm (Fig. 6). The corresponding necessary parameters (L, n) for the strength scaling equation are given in Table 3.

Table 3 Setup parameters for the three chosen four-line bending configurations

	Outer span L [mm]	Inner span l [mm]	$n = \frac{L-l}{2L}$
Configuration 1	60	32	$^{7}/_{30}$
Configuration 2	80	48	$^{1}/_{5}$
Configuration 3	100	70	$^{3}/_{20}$

It should be noted here that the third configuration (100-70 mm) is fairly close to the geometrical limits explained in the previous paragraph. Indeed, as can be seen in Fig. 6.c, because of the very large bending radius imposed by the dimensions of the setup, the wafer will “fall” from the supports before reaching its maximum bending position. The authors thus remind that this configuration should never be used for accurate silicon wafer strength evaluation and that it was only chosen in this study for the purpose(s) of illustrating the strength size effect.

(a) 60-32 mm configuration

(b) 80-48 mm configuration

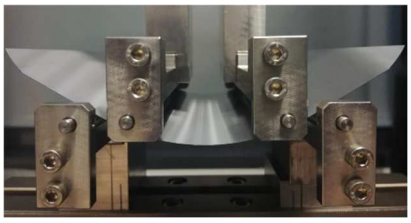

(c) 100-70 mm configuration

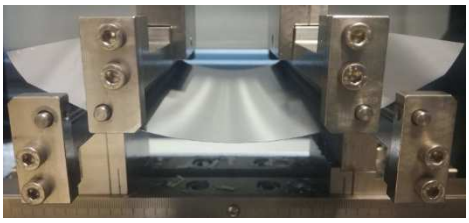

Fig. 6 The three configurations used for the four-line bending tests

The 240 wafers were alternately sampled in three series of 80 wafers for each configuration. Furthermore, to account for the surface anisotropy of the diamond-wire sawn wafers [36], each set was divided into two subsets to be tested either with the saw marks parallel or perpendicular to the loading rollers (thereafter referred to as wire direction and cut direction, as illustrated in Fig. 7).

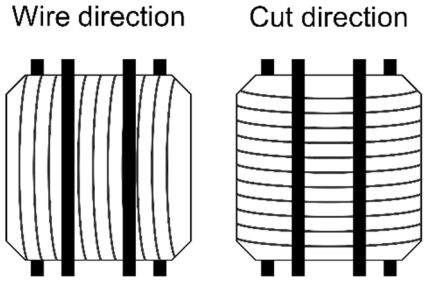

Fig. 7 Testing configuration depending on the orientation of the loading rollers with respect to saw marks

For a given setup configuration, 40 wafers per direction were tested until fracture. A low crosshead speed rate of 10 mm/min is used, which corresponds to a strain rate in the order of 10^{-5} s^{-1} and thus ensures a quasi-static loading condition. It is worth noting that this speed is in agreement with the recommendations of [15]. In order to relieve frictional constraints and according to the recommendations of [7], the loading and support rollers are free to rotate about their axis.

Moreover, the upper loading rollers can independently articulate to match the wafer top surface, and only one of the two support rollers can articulate while the other is fixed. An initial 1 N preload is imposed in order to remove slack from the load string while the rollers articulate and to facilitate the processing and comparison of the load-deflection curves, which are the main raw results (Fig. 9).

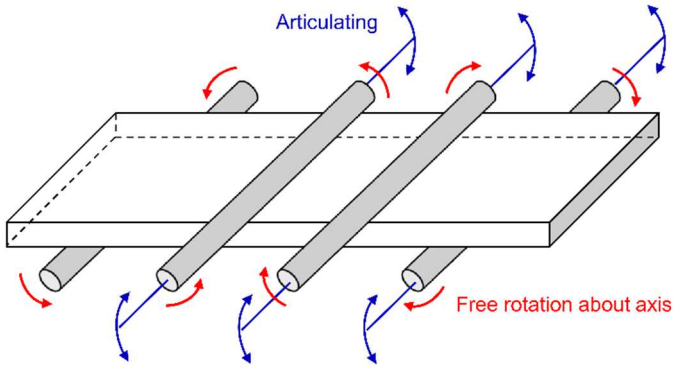

Fig. 8. Schematic figure of a fully-articulated bending fixture according to [7]. The two loading rollers are free to roll and they can independently articulate to match the wafer top surface. The two loading rollers are free to roll, and one can articulate to match the wafer bottom surface.

As expected, Fig. 9 reveals that the mean slope of the load-deflection curves is the highest for the 60-32 mm configuration and the lowest for the 100-70 mm configuration. A comparison of the curves obtained in cut and wire direction (Fig. 9 (a) and (b), respectively) confirms the well-known dependency of the mechanical properties of diamond-sawn wafers with respect to the orientation of the saw marks: the maximum deflection values and fracture loads reached in *wire direction* are much lower than in *cut direction*.

It can also be pointed out that the curves obtained from 100-70 mm configuration in cut direction exhibit some irregular oscillations, especially for deflections higher than 10 mm. These oscillations are the result of a “stick-slip” phenomenon between the wafers’ lower surface and the lower supports, which is very likely due to the aforementioned geometrical limits of this configuration.

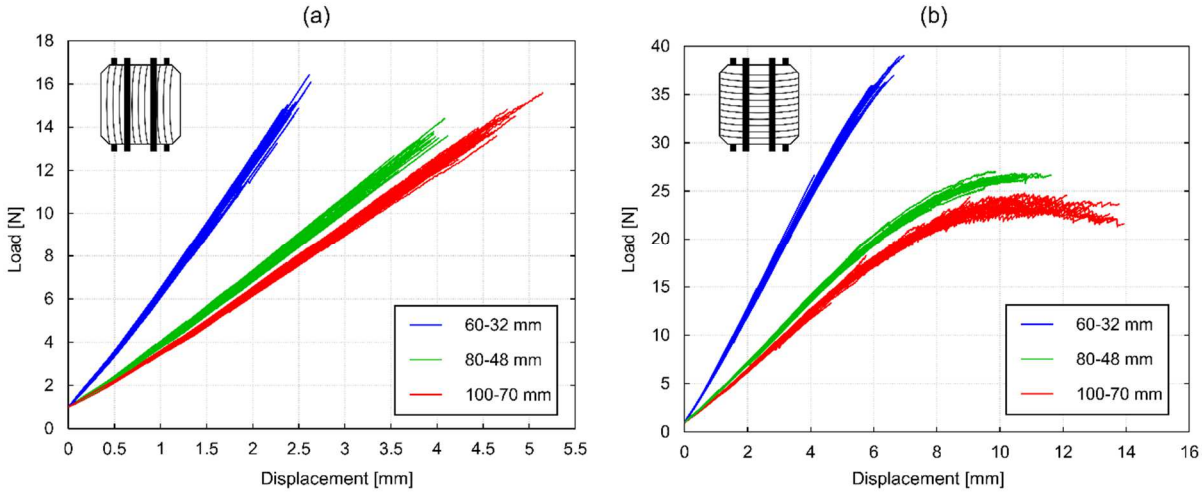

Fig. 9 Load-deflection curves obtained for the three testing configurations in (a) wire direction and (b) cut direction (40 wafers of average thickness 179 µm per series)

3.3 Finite element modeling

The curves from Fig. 9 also illustrate that beyond a certain deflection value, the relationship between load and displacement stops being linear and the force measured by the cell decreases. The reason for this is that with increasing crosshead displacement, the contact surface between wafer and roller, which was initially horizontal, becomes slanted and even near-vertical. The

vertical component of the load measured by the load cell thus decreases in favor of the horizontal component. This effect is particularly significant for the 80-48 mm and 100-70 mm configurations. Because of this non-linearity, the analytical formulas expressing stress as a function of displacement cannot be considered as valid to evaluate the stresses in the moment of failure. Finite element (FE) models of the experimental setups were therefore developed on ANSYS software in order to obtain the stress distribution in the samples at the time of fracture.

One model was built for each configuration. In all cases, the double-symmetry of the setup was used to simplify the calculation and only a quarter of the geometry was modeled in 3D (Fig. 10). The silicon wafer is meshed with quadratic cubic elements with four layers along the thickness. Because the mesh was refined in the contact areas, whose dimensions slightly differ between the configurations, the total number of elements for the wafer is not the same for the three models (Table 4).

The loading rollers are considered as semi-cylindrical rigid surfaces. The support rollers are fixed in all degrees of freedom and a displacement is imposed on the loading rollers. Based on the maximum failure deflection values δ_{max} reached experimentally, a different total displacement was imposed for each configuration (Table 4). The frictional contact between rollers and wafer surface is computed with a friction coefficient of f = 0.12, which showed the best agreement between the numerical and experimental load-deflection curves. Because silicon is a brittle material, the failure criterion used to determine the fracture stress is the maximum principal stress.

Table 4 Number of mesh elements and maximum displacement imposed in the numerical model depending on configuration

Configuration	Number of elements in wafer mesh	Maximum displacement imposed δ_{max}
60-32 mm	29 520	7 mm
80-48 mm	25 200	12 mm
100-70 mm	29 760	15 mm

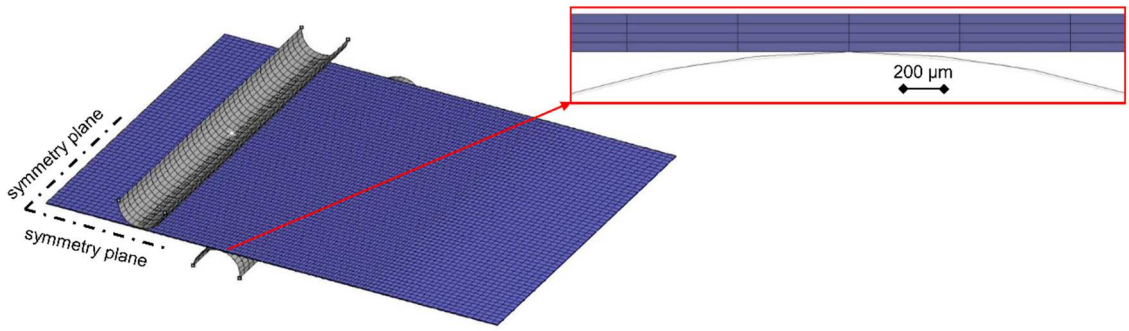

Fig. 10 Global mesh used for the FE model of the 60-32 mm configuration and zoom on the lower contact area

Fig. 11 shows the distribution of the normalized maximum principal stress at the bottom surface and along the wafer length for the three configurations, for a given wafer thickness (180 µm) and displacement values ranging from $\delta_{max}/_4$ to δ_{max}. For all configurations, the stress is zero outside the supports rollers and maximal between the loading rollers. It is worth noting that the stress field is not strictly constant along the wafer length but instead slightly increases from the wafer center to the area under the upper (central) rollers. Moreover, this inhomogeneity increases with increasing wafer deflection. For the 80-48 mm and 60-32 mm configurations, the differences remain respectively below 6% and 4% at the maximum displacement values and can be considered negligible. For the 100-70 mm configuration however, the difference between the stress at the center and the stress below the upper (central) rollers is already around 10% for $\delta_{max}/_2$ and over

18% for the maximum displacement. This is a result of the high span ratio chosen for this configuration ($^{l}/_{L}$= 0.7).

Indeed, the problem of the stress increasing towards the end of the pure bending section in a four-line bending setup is not new and has already been highlighted by several studies [48,49]. This effect, often designated as wedging stress, arises from load application on the surface of the specimen and not over the cross section [50]. For a given outer span L, increasing the inner span l will increase the wedging stress and therefore lead to inhomogeneous stress fields [15,49]. However, choosing a high span ratio was necessary in this study in order to obtain significant differences in effective volumes between the configurations.

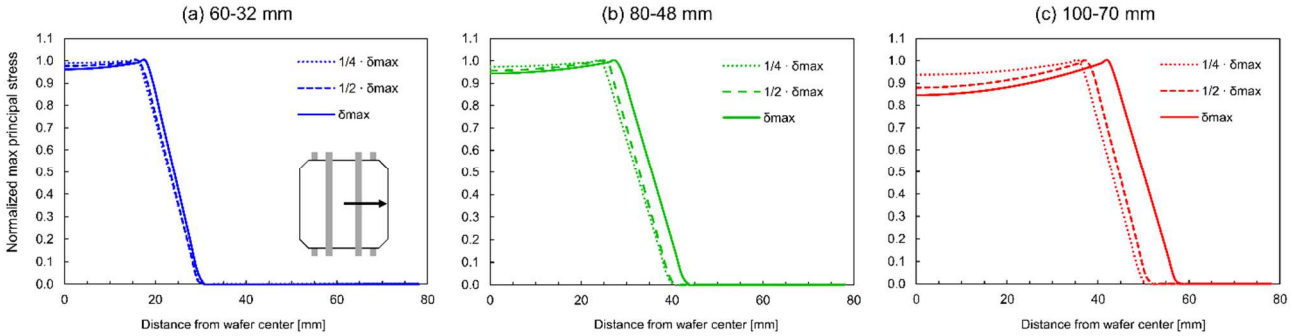

Fig. 11 Normalized maximum principal stress at the bottom surface and along the wafer length obtained by FE simulations for a given thickness (180 µm) and different displacement values for the configurations (a) 60-32 mm (b) 80-48mm (c) 100-70 mm

In order to reduce calculation time, only five thicknesses within the measured range of the series were simulated for each configuration to obtain the relation between maximum stress and displacement, and the results for the other thicknesses were interpolated.

3.4 Weibull parameters estimation

The stress values obtained by FE calculation for each series are rearranged in ascending order so as to be displayed graphically. Since it is impossible to know the true value of the corresponding probability P_i for each measured σ_i from the experiments, a prescribed function should be employed to calculate the P_i-value. Such a prescribed function is called the probability index. Different forms of probability indexes have been proposed, which usually start from the following general form:

$$P(\sigma_i) = \frac{i - \alpha}{N + \beta} \tag{17}$$

where N is he total number of samples per series. Several studies have been reported aiming to find suitable values for the parameters α and β that minimize the bias of the estimated Weibull modulus m [51–53]. This biased estimation is however only an issue if the Weibull modulus is estimated via the least square regression method [54]. In this study, we choose to estimate the Weibull parameters by the maximum likelihood method, which does not require the use of probability indexes. The probability index is therefore only used for graphical representation (experimental scatterplot of P_i vs σ_i). We choose to compute the failure probability P_i via Bénard's approximation for median ranks:

$$P(\sigma_i) = \frac{i - 0.3}{N + 0.4} \tag{18}$$

Where N is the total number of samples per series. As introduced in the theoretical part, we chose to fit the stress values σ_i to a two-parameter Weibull distribution, in which the probability of failure P_f at an applied stress σ is defined as:

$$P_f(\sigma) = 1 - exp\left[-\left(\frac{\sigma}{\sigma_\theta}\right)^m\right] \quad (19)$$

Where σ_θ is the characteristic fracture strength, which is dependent on the size of the sample and m is the Weibull modulus, which is a material constant and should therefore remain constant whatever the configuration used. The Weibull parameters were estimated with their confidence bounds and the corresponding contour plots were calculated using the likelihood ratio method for a confidence level of 90%.

4 Results and discussion

4.1 Weibull parameters

The Weibull parameters estimated for the three configurations in both testing directions are given in Table 5 and depicted as probability plots in Fig. 12. Moreover, in order to better visualize the statistical significance of the obtained values, Fig. 13 shows the 90% confidence contour plots for the estimated Weibull parameters. Several observations can be drawn from the values and corresponding graphs obtained. Firstly and as expected, for a given configuration and testing direction, silicon wafers exhibit characteristic strength values that are in average two times higher in cut direction than in wire direction. This difference in strength is accompanied by a difference in the scattering of the results, with a calculated Weibull modulus in wire direction on average twice the one from wafers tested in cut direction. This observation is valid for all three configurations and is a characteristic property of DWS wafers. An interpretation of this double anisotropy in strength and modulus, based on the orientation of the stress with respect to the characteristic defects, can be found in a previous study [46] and will not be further detailed here.

Table 5 Weibull parameters of strength with 90% confidence bounds for the three different configurations in wire and cut direction

Configuration	Testing direction	Characteristic fracture strength σ_θ [MPa]	Weibull modulus m [-]
60-32 mm	Wire	123 (121 … 125)	16.5 (13.3 … 20.0)
	Cut	285 (276 … 294)	8.6 (6.9 … 10.6)
80-48 mm	Wire	122 (120 … 124)	16.5 (13.2 … 20.2)
	Cut	267 (258 … 275)	8.6 (6.9 … 10.6)
100-70 mm	Wire	119 (117 … 121)	16.1 (13.0 … 19.4)
	Cut	242 (231 … 253)	6.2 (4.9 … 7.6)

An important finding is however that regardless of the inner and outer span of the four-line bending setup, the Weibull modulus estimated stays constant for a given testing direction. This indicates this parameter is indeed a constant representative of the critical defect distribution in the wafer, which only depends on the testing direction and not on the size of the tested sample. Although its value remains within the 90% confidence bounds (Fig. 13), one might argue that the estimated Weibull modulus is slightly lower for the 100-70 mm configuration in cut direction. This could be explained by the inhomogeneous stress field generated at the wafer surface for this configuration, which can increase the scattering of the results and therefore decrease the estimated Weibull modulus. Indeed, the 100-70 mm configuration is not only the setup which exhibits the most inhomogeneous stress field, but also the setup for which the highest deflections are reached. More than one quarter of the wafers fail at displacement values higher than 12 mm, at which the difference in stress at the wafer center exceeds 18%.

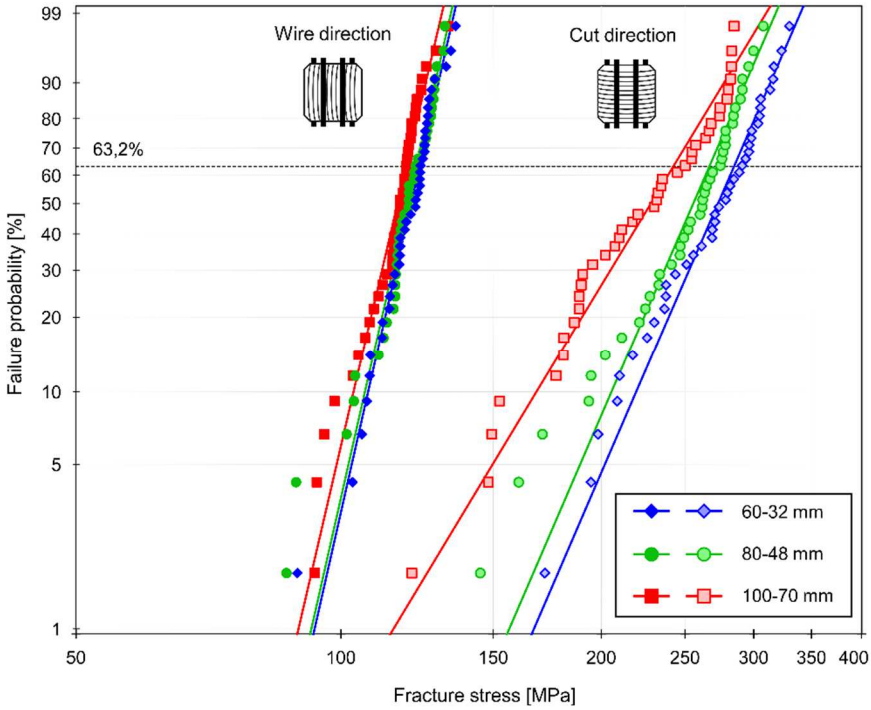

Fig. 12 Weibull probability failure plots for the three setup configurations in wire and cut direction

The strength values then confirm that DWS wafers do exhibit a significant size effect. Indeed, when testing the wafers perpendicular to the saw mark (*cut direction*) the estimated characteristic strength σ_θ is respectively 10% and 18% higher for the 80-48 mm and 60-32 mm configurations than for the 100-70 mm configuration. In the *wire direction* however, the observed size effect is much weaker or even nonexistent when considering the 90% confidence bounds. The reason for this is a direct consequence of the anisotropy in Weibull modulus depending on the testing direction. Indeed, as recalled by the strength scaling equation developed in the previous part, size effect depends on the effective length of the chosen setup and on Weibull modulus value m:

$$\frac{\sigma_{\theta 2}}{\sigma_{\theta 1}} = \left(\frac{L_{\text{eff},1}}{L_{\text{eff},2}}\right)^{\frac{1}{m}} \tag{20}$$

The strength size effect is thus much stronger in *cut direction* because the Weibull modulus is lower, i.e. because the characteristic defects in this direction have a stronger dispersion. Reducing the size of the tested sample decreases the probability of finding a highly critical defect and thus increases the characteristic strength.

(a) Wire direction

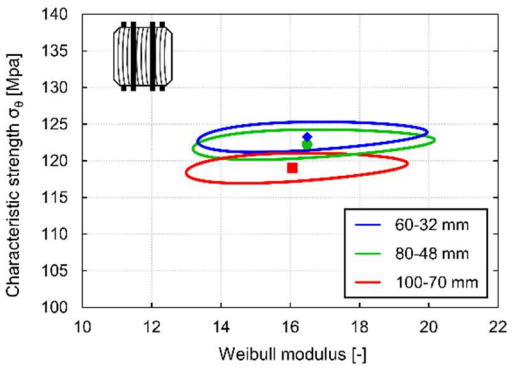

(b) Cut direction

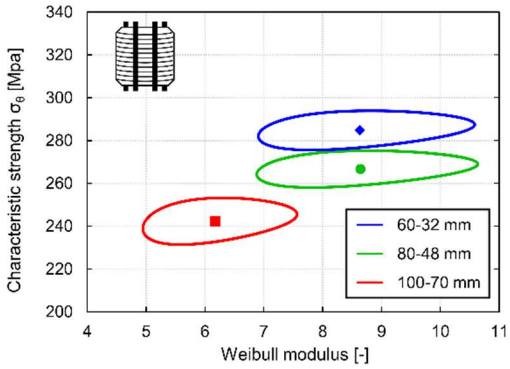

Fig. 13 Weibull 90% confidence contour plots for the three configurations in (a) wire direction and (b) cut direction

4.2 Validity of the strength scaling law for silicon wafers

The goal of this section is to check whether the strength scaling law from equation (20) can accurately describe the strength size effect observed when testing DWS silicon wafers. As a first step, we compute the effective length of each configuration, which as demonstrated in the introduction, depends on the four-line bending setup parameters (L, n) and the Weibull modulus m:

$$L_{\text{eff}} = 2L \times \frac{m + 1 - 2nm}{m + 1} \tag{21}$$

Based on the estimation method of the Weibull modulus, we can define 90% confidence bounds for the effective length parameter. The lower bound for L_{eff} is calculated using the 90% upper bound of Weibull modulus in equation (21) and vice versa. The calculated values for L_{eff} and corresponding confidence bounds are given in Table 6.

Table 6 Effective length and corresponding 90% confidence bounds estimated from Weibull moduli for the three configurations and two testing directions

Testing direction	Configuration	Weibull modulus [-]	L_{eff} [mm]
Cut	100-70 mm	6.2 (5.0 … 7.6)	20.7 (17.0 … 25.0)
	80-48 mm	8.6 (7.0 … 10.7)	10.6 (8.6 … 13.1)
	60-32 mm	8.6 (7.0 … 10.7)	7.2 (5.9 … 8.9)
Wire	100-70 mm	16.1 (13.2 … 19.6)	8.4 (6.9 … 10.2)
	80-48 mm	16.5 (13.3 … 20.4)	5.7 (4.6 … 7.0)
	60-32 mm	16.5 (13.5 … 20.2)	3.8 (3.1 … 4.7)

The validity of the strength scaling equation can then be evaluated by two methods: first by comparing its accuracy in describing the “mean Weibull modulus” of the series of wafers, and second by its ability to predict the evolution of the strength from one setup configuration to another.

1) Mean Weibull modulus of the strength scaling equation

In this first analysis, we plot the effective length L_{eff} as a function of the characteristic strength σ_θ on a double-logarithmic scale for both testing directions, as illustrated in Fig. 14. Indeed, we can rearrange equation (20) to get:

$$ln\left(\frac{L_{\text{eff},1}}{L_{\text{eff},2}}\right) = -m \times ln\left(\frac{\sigma_{\theta 1}}{\sigma_{\theta 2}}\right) \tag{22}$$

This expression shows that the logarithm of the effective length $ln(L_{\text{eff}})$ should decrease linearly with the logarithm of the characteristic strength $ln(\sigma_\theta)$. The slope of the obtained curve is equal to m, which corresponds to the "mean Weibull modulus" [35,55] of the tested silicon wafers, a parameter that remains constant regardless of the effective length. This slope was evaluated by the least square method for each testing direction. The values obtained, thereafter referred to as $\hat{m}_{cut}$ and $\hat{m}_{wire}$, are indicated on the graph from Fig. 14 along with the coefficient of determination R^2, which is an indicator of the goodness of fit of the strength scaling equation to our experimental data. Moreover, if the size effect equation (22) is correct, then the values $\hat{m}_{cut}$ and $\hat{m}_{wire}$ should be close to the arithmetic means of the three estimated individual moduli, i.e. for each direction:

$$\overline{m}_{cut} = \frac{6.2 + 8.6 + 8.6}{3} = 7.8$$
$$\overline{m}_{wire} = \frac{16.1 + 16.5 + 16.5}{3} = 16.3 \quad (23)$$

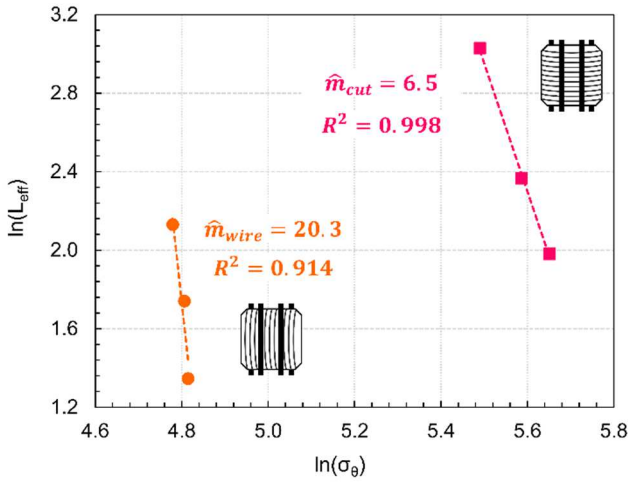

Fig. 14 Correlation between characteristic strength and effective length and evaluation of the mean Weibull modulus for each testing direction (least square method)

It can be seen that in *cut direction,* the regression curve fits the experimental points very well, but the mean value $\hat{m}_{cut}$ of 6.5 obtained is lower than the arithmetic mean $\overline{m}_{cut}$ of 7.8. This deviation is not a result of the lower Weibull modulus obtained for the 100-70 mm configuration, because if we were to compute the regression curve with only the experimental values from the 80-48 mm and 60-32 mm configuration, the calculated mean value $\hat{m}_{cut}$ would be of 5.9. In other words, the stress values obtained for the three configurations would normally imply a lower Weibull modulus than the one obtained by the maximum likelihood method estimation from 40 samples.

In wire direction, the regression curve does not fit the experimental points as well as in cut direction, as indicated by lower value of R^2. More specifically, the mean value $\hat{m}_{wire}$ of 20.3 obtained by the least square method is overestimated compared to the arithmetic average of 16.3. The effect is therefore the exact opposite of what is observable in *cut direction*: the measured experimental strength values in *wire direction* show almost no dependence on the size effect, which should normally imply a higher Weibull modulus value than the one obtained by the maximum likelihood method estimation from 40 samples.

These results indicate that the Weibull modulus estimated by the maximum likelihood method based on the results from one testing configuration could be biased. On the one hand, in the case where the value is relatively low, such as in *cut direction*, the number of samples is probably too small to obtain a reliable value and the Weibull modulus can change depending on the testing configuration. In *wire direction*, where the Weibull modulus is on the other hand quite high, the value might be underestimated. A more precise way to determine this parameter as an actual material constant independent of the tested size, would be to perform tests with different setup

configurations, and to determine the mean Weibull modulus $\hat{m}$, as was done in this section. The value obtained with this procedure would have a more physical meaning. It should however be noted that for strength evaluation of PV silicon wafers, the parameter of highest importance is usually rather the reference strength σ_θ.

2) Predicting strength as a function of effective length

An alternative way to check whether the strength scaling law accurately describes the size effect observed for the three configurations is to compare the size effect prediction based on each configuration. Indeed, from the estimated Weibull parameters σ_θ and m from Table 5 and the calculated effective length from Table 6, it is possible to derive, for each configuration, the expression predicting the characteristic reference strength σ_0 of a sample as a function of its effective length L_0. For example, the expression predicting the characteristic reference strength in cut direction based on the results from configuration 100-70 mm is as follows:

$$\sigma_{0,cut} = \sigma_{\theta,cut,100-70mm} \times \left(\frac{L_{eff,cut,100-70mm}}{L_0}\right)^{\frac{1}{m_{cut,100-70mm}}} \quad (24)$$

Following this reasoning, we can derive the strength scaling expressions for each testing direction of the three configurations, and compare them by showing the evolution of the reference strength σ_0 as a function of reference length L_0. This is illustrated in Fig. 15 for values of L_0 between 1 and 500 mm. The uncertainty bars in the graphs are obtained by computing the reference strength value σ_0 with either the upper or lower bound for L_{eff} (as given in Table 6).

Fig. 15.a highlights that in *wire direction*, the three scaling equations overlap for the considered values, thus meaning that the strength scaling law derived in the introduction predicts the stress distribution correctly for the three configurations. This result could of course be expected since the stress distribution values barely change from one configuration to another.

In *cut direction* however, the strength scaling laws obtained from the results for configuration 60-32 mm and 80-48 mm almost perfectly overlap for a range of values between 1 and 500 mm. The evolution of strength estimated by the results from configuration 100-700 mm is however shifted towards lower values. This implies two things:

(i) If we were to predict the stress distribution values for the 100-70 mm configuration based on the results from the two other configurations, the estimated values would be overestimated in comparison with the experimental ones.

(ii) If we were to predict the stress distribution values for the 80-48 mm configuration (or the 60-32 mm configuration) based on the results from the 100-70 mm configuration, the estimated values would be underestimated in comparison with the experimental ones.

These two observations are naturally correlated and reflect the fact that the stress distribution obtained with the 100-70 mm in *cut direction* does not fit the strength scaling equation, while the two other configurations do. The main hypothesis to explain why this is only observable in *cut direction* and not in *wire direction* is that, as mentioned in previously, the inhomogeneity of the stress field increases with wafer deflection. When testing the wafers in wire direction, the failure deflection values remain below 5 mm for all configurations and the influence of an inhomogeneous stress field can be avoided. This finding thus sets first limits to the applicability of the strength scaling equations for silicon wafers: the testing conditions need to ensure a homogeneous stress field along with relatively small deflection at failure.

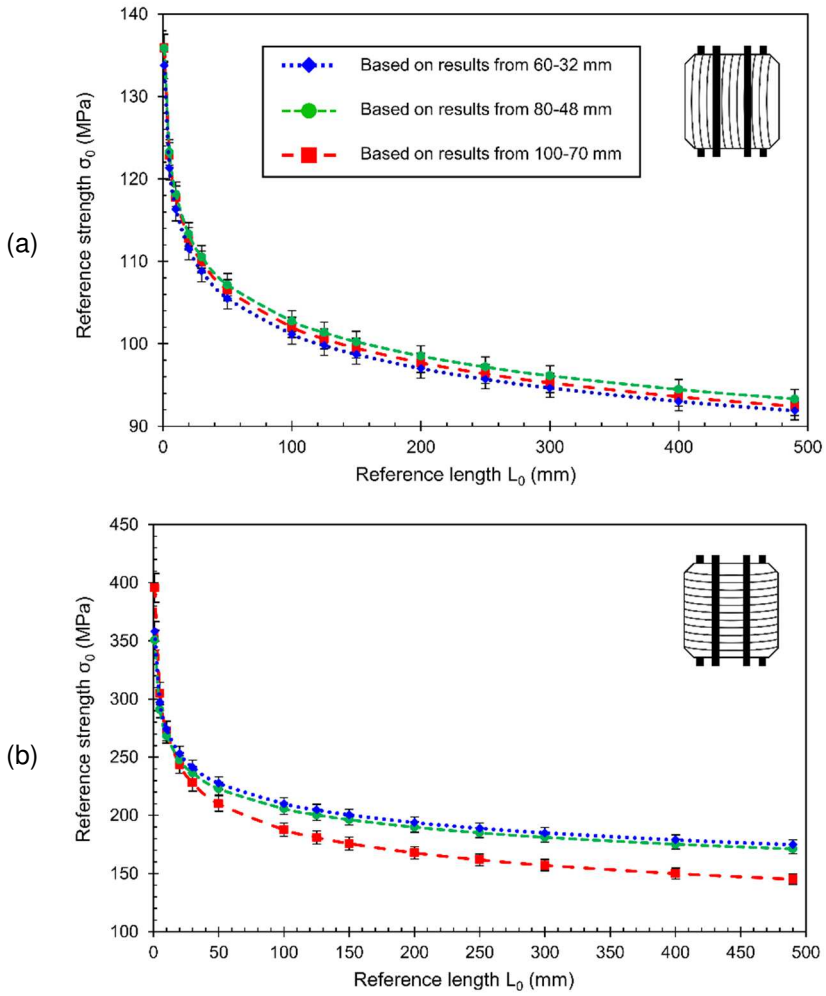

Fig. 15. Strength scaling laws predicting the evolution of reference strength σ_0 as a function of reference length L_0 in (a) wire direction and (b) cut direction based on results obtained with the three configurations

5 Conclusions and prospects

The main goal of this study was to shed some light on the existence of a Weibull strength size effect when testing diamond wire sawn silicon wafers. We first derived an analytical strength scaling law based on the specific geometry of thin silicon wafers tested in a four-line bending setup, and showed that the expression was identical regardless of the assumption made on the type of defect population and depended only on the dimensions of the setup and the Weibull modulus of the stress population. The validity of this scaling law was then investigated experimentally, by comparing the Weibull stress distribution results of monocrystalline silicon wafers obtained for three configurations of bending setups.

The main finding of this experimental study is that DWS wafers exhibit an anisotropic behavior with respect to Weibull strength size effect: when bent in *cut direction*, the fracture strength values increase with decreasing effective length. When bent in *wire direction* however, the stress distribution remains the same regardless of the setup configuration. This result is an experimental validation that the strength size effect depends on the scattering of the defect population, i.e. on the Weibull modulus. The theoretical scaling law developed was found to accurately describe the strength size effect for two of the setup configurations but was inadequate for the configuration with span configuration 70-100 mm, mainly because of the highly inhomogeneous stress field generated in the wafer at high deflection values.

These findings open up prospects for further standardization of wafer strength evaluation for the PV industry, more specifically for diamond-wire sawn wafers, which now account for all of the

monocrystalline-based solar cells. Indeed, we highlighted that it is inaccurate to directly compare strength parameters obtained from different setup dimensions when testing wafers perpendicular to the diamond saw marks. One could recommend using the Weibull strength scaling law developed in this study to compute reference strengths that would then be comparable. We showed however that in cases where very high wafer deflections values are reached before failure, the inhomogeneous generated stress field may lead to bias assessment of the strength scaling law.

The best recommendation to obtain directly comparable wafer strength values would therefore be to limit the results to bending tests performed parallel to the wire saw marks. Indeed, results show that failure stress values obtained when bending wafers in the wire direction should not vary with the setup dimensions. This recommendation is also of practical value, since this loading direction is precisely the most critical one for DWS wafers. This points to the possibility of developing a standard for strength testing of DWS photovoltaic wafers, which would recommend testing the samples only in the direction of the saw marks.

References

[1] International Technology Roadmap for Photovoltaic (ITRPV), 10th edition, 2019.

[2] A. Kumar, S. Melkote, Diamond wire sawing of solar silicon wafers: a sustainable manufacturing alternative to loose abrasive slurry sawing, in: 15th Global Conference on Sustainable Manufacturing, Elsevier, 2018: pp. 549–566. https://doi.org/10.1016/j.promfg.2018.02.156.

[3] F. Coustier, R. Riva, M. Debourdeau, N. Velet, J. Bounan, A. Chabli, Diamond wire process monitoring, Photovoltaics International. 39 (2018) 34–40.

[4] H. Sekhar, T. Fukuda, K. Tanahashi, H. Takato, The impact of silicon brick polishing on thin (120 µm) silicon wafer sawing yields and fracture strengths in diamond-wire sawing, Materials Science in Semiconductor Processing. 105 (2020) 104751. https://doi.org/10.1016/j.mssp.2019.104751.

[5] R. Koepge, K. Buehler, A. Langhans, F. Kaule, E. Velispahic, Variation of silicon wafer strength and edge chipping induced by residual stresses at the brick bonding interface, in: Proceedings of the 36th European Photovoltaic Solar Energy Conference, 2019.

[6] X. Li, T. Kasai, S. Nakao, T. Ando, M. Shikida, K. Sato, H. Tanaka, Anisotropy in fracture of single crystal silicon film characterized under uniaxial tensile condition, Sensors and Actuators A: Physical. 117 (2005) 143–150. https://doi.org/10.1016/j.sna.2004.06.003.

[7] ASTM International, Standard Test Method for Flexural Strength of Advanced Ceramics at Ambient Temperature, ASTM C 1161, (2018).

[8] V.A. Popovich, A.C. Riemslag, M. Janssen, I.J. Bennett, I.M. Richardson, Characterization of multicrystalline silicon solar wafers fracture strength and influencing factors, International Journal of Material Science. 3 (2013).

[9] L. Zhao, A. Maynadier, D. Nelias, Stiffness and fracture analysis of photovoltaic grade silicon plates, International Journal of Solids and Structures. 97–98 (2016) 355–369. https://doi.org/10.1016/j.ijsolstr.2016.07.013.

[10] A.S. Azar, B. Holme, Ø. Nielsen, Effect of sawing induced micro-crack orientations on fracture properties of silicon wafers, Engineering Fracture Mechanics. 154 (2016) 262–271. https://doi.org/10.1016/j.engfracmech.2016.01.014.

[11] C. Yang, F. Mess, K. Skenes, S. Melkote, S. Danyluk, On the residual stress and fracture strength of crystalline silicon wafers, Applied Physics Letters. 102 (2013) 021909. https://doi.org/10.1063/1.4776706.

[12] D. Echizenya, K. Sasaki, Effect of surface damage on strength of silicon wafer for solar cells, in: Electronics Packaging (ICEP), 2014 International Conference On, IEEE, 2014: pp. 14–18.

[13] K. Yuan, Y. Sun, Y. Lu, X. Liang, D. Tian, X. Ma, D. Yang, Comparison on mechanical properties of heavily phosphorus- and arsenic-doped Czochralski silicon wafers, AIP Advances. 8 (2018) 045301. https://doi.org/10.1063/1.5025516.

[14] S. Saffar, S. Gouttebroze, Z.L. Zhang, Fracture Analysis and Distribution of Surface Cracks in Multicrystalline Silicon Wafers, Journal of Solar Energy Engineering. 136 (2014) 021024.

[15] DIN SPEC 91351: Strength testing for photovoltaic wafers, (2017).

[16] F. Kaule, B. Köhler, J. Hirsch, S. Schoenfelder, D. Lausch, Improved mechanical strength and reflectance of diamond wire sawn multi-crystalline silicon wafers by inductively coupled plasma (ICP) etching, Solar Energy Materials and Solar Cells. 185 (2018) 511–516. https://doi.org/10.1016/j.solmat.2018.05.057.

[17] W. Weibull, A statistical distribution function of wide applicability, Journal of Applied Physics. 18 (1951) 293–297.

[18] J. Barredo, V. Parra, I. Guerrero, A. Fraile, L. Hermanns, On the mechanical strength of monocrystalline, multicrystalline and quasi-monocrystalline silicon wafers: a four-line bending test study, Progress in Photovoltaics: Research and Applications. (2013) n/a-n/a. https://doi.org/10.1002/pip.2372.

[19] S.F. Duffy, E.H. Baker, A.A. Wereszczak, J.J. Swab, Weibull Analysis Effective Volume and Effective Area for a Ceramic C-Ring Test Specimen, Journal of Testing and Evaluation. 33 (2005) 233–238.

[20] G.D. Quinn, Weibull strength scaling for standardized rectangular flexure specimens, Journal of the American Ceramic Society. 86 (2003) 508–510.

[21] C. Yang, H. Wu, S. Melkote, S. Danyluk, Comparative Analysis of Fracture Strength of Slurry and Diamond Wire Sawn Multicrystalline Silicon Solar Wafers, Advanced Engineering Materials. 15 (2013) 358–365. https://doi.org/10.1002/adem.201200262.

[22] H. Meng, L. Zhou, Mechanical Behavior of Diamond-Sawn Multi-Crystalline Silicon Wafers and its Improvement, Silicon. 6 (2014) 129–135. https://doi.org/10.1007/s12633-013-9170-2.

[23] R. Danzer, P. Supancic, J. Pascual, T. Lube, Fracture statistics of ceramics - Weibull statistics and deviations from Weibull statistics, Engineering Fracture Mechanics. 74 (2006) 2919–2932.

[24] M. Ambroži, R.A. Bermejo, P.H. Supancic, T. Kosma, Monte Carlo simulation of Weibull distribution of ceramic strength values, in: 2008.

[25] R. Danzer, On the relationship between ceramic strength and the requirements for mechanical design, Journal of the European Ceramic Society. 34 (2014) 3435–3460. https://doi.org/10.1016/j.jeurceramsoc.2014.04.026.

[26] F.W. Zok, On weakest link theory and Weibull statistics, Journal of the American Ceramic Society. 100 (2017) 1265–1267. https://doi.org/10.1111/jace.14665.

[27] R. Danzer, A general strength distribution function for brittle materials, Journal of the European Ceramic Society. 10 (1992) 461–472.

[28] W. Weibull, A statistical theory of the strength of materials, Royal Swedish Institute for Engineering Research. (1939) 1–45.

[29] K. Trustrum, A.D.S. Jayatilaka, On estimating the Weibull modulus for a brittle material, J Mater Sci. 14 (1979) 1080–1084. https://doi.org/10.1007/BF00561290.

[30] C. Lu, R. Danzer, F.D. Fischer, Influence of Threshold Stress on the Estimation of the Weibull Statistics, Journal of the American Ceramic Society. 85 (2002) 1640–1642.

[31] B. Deng, D. Jiang, J. Gong, Is a three-parameter Weibull function really necessary for the characterization of the statistical variation of the strength of brittle ceramics?, Journal of the European Ceramic Society. 38 (2018) 2234–2242. https://doi.org/10.1016/j.jeurceramsoc.2017.10.017.

[32] J. Malzbender, R.W. Steinbrech, Threshold fracture stress of thin ceramic components, Journal of the European Ceramic Society. 28 (2008) 247–252. https://doi.org/10.1016/j.jeurceramsoc.2007.05.017.

[33] M.E. Saleh, J.L. Beuth, M.P. Boer, Validated Prediction of the Strength Size Effect in Polycrystalline Silicon Using the Three-Parameter Weibull Function, Journal of the American Ceramic Society. 97 (2014) 3982–3990.

[34] C. Przybilla, A. Fernández-Canteli, E. Castillo, Deriving the primary cumulative distribution function of fracture stress for brittle materials from 3- and 4-point bending tests, Journal of the European Ceramic Society. 31 (2011) 451–460. https://doi.org/10.1016/j.jeurceramsoc.2010.11.007.

[35] H. Fischer, W. Rentzsch, R. Marx, A modified size effect model for brittle nonmetallic materials, Engineering Fracture Mechanics. 69 (2002) 781–791.

[36] A. Bidiville, K. Wasmer, R. Kraft, C. Ballif, Diamond wire-sawn silicon wafers-from the lab to the cell production, in: Proceedings of the 24th EU PV-SEC, 2009: pp. 1400–1405.

[37] T. Suzuki, Y. Nishino, J. Yan, Mechanisms of material removal and subsurface damage in fixed-abrasive diamond wire slicing of single-crystalline silicon, Precision Engineering. 50 (2017) 32–43. https://doi.org/10.1016/j.precisioneng.2017.04.011.

[38] A. Kumar, S. Kaminski, S.N. Melkote, C. Arcona, Effect of wear of diamond wire on surface morphology, roughness and subsurface damage of silicon wafers, Wear. 364–365 (2016) 163–168. https://doi.org/10.1016/j.wear.2016.07.009.

[39] H. Xiao, H. Wang, N. Yu, R. Liang, Z. Tong, Z. Chen, J. Wang, Evaluation of fixed abrasive diamond wire sawing induced subsurface damage of solar silicon wafers, Journal of Materials Processing Technology. 273 (2019) 116267. https://doi.org/10.1016/j.jmatprotec.2019.116267.

[40] T. Liu, P. Ge, W. Bi, Y. Gao, Subsurface crack damage in silicon wafers induced by resin bonded diamond wire sawing, Materials Science in Semiconductor Processing. 57 (2017) 147–156. https://doi.org/10.1016/j.mssp.2016.10.021.

[41] A. Kumar, R.G.R. Prasath, V. Pogue, K. Skenes, C. Yang, S.N. Melkote, S. Danyluk, Effect of Growth Rate and Wafering on Residual Stress of Diamond Wire Sawn Silicon Wafers, Procedia Manufacturing. 5 (2016) 1382–1393. https://doi.org/10.1016/j.promfg.2016.08.108.

[42] A. Kumar, C. Yang, S. Melkote, S. Danyluk, Relationship between Macro- scale and Micro-scale Mechanical Properties of Photovoltaic Silicon wafers, in: Proceedings of the 29th European Photovoltaic Solar Energy Conference and Exhibition EU PVSEC, 2014: pp. 769–772.

[43] P. Wang, X. Yu, Z. Li, D. Yang, Improved fracture strength of multicrystalline silicon by germanium doping, Journal of Crystal Growth. 318 (2011) 230–233. https://doi.org/10.1016/j.jcrysgro.2010.11.081.

[44] R. Danzer, T. Lube, P. Supancic, R. Damani, Fracture of Ceramics, in: Ceramics Science and Technology, John Wiley & Sons, Ltd, 2010: pp. 529–575. https://doi.org/10.1002/9783527631735.ch12.

[45] J. Schijve, ed., Stress Intensity Factors of Cracks, in: Fatigue of Structures and Materials, Springer Netherlands, Dordrecht, 2009: pp. 105–140. https://doi.org/10.1007/978-1-4020-6808-9_5.

[46] L. Carton, R. Riva, D. Nelias, M. Fourmeau, F. Coustier, A. Chabli, Comparative analysis of mechanical strength of diamond-sawn silicon wafers depending on saw mark orientation, crystalline nature and thickness, Solar Energy Materials and Solar Cells. 201 (2019) 110068. https://doi.org/10.1016/j.solmat.2019.110068.

[47] A. Bhushan, S.K. Panda, D. Khan, A. Ojha, K. Chattopadhyay, H.S. Kushwaha, I.A. Khan, Weibull Effective Volumes, Surfaces, and Strength Scaling for Cylindrical Flexure Specimens Having Bi-Modularity, JTE. 44 (2016) 1978–1997. https://doi.org/10.1520/JTE20150301.

[48] T. Zhai, Y.G. Xu, J.W. Martin, A.J. Wilkinson, G.A.D. Briggs, A self-aligning four-point bend testing rig and sample geometry effect in four-point bend fatigue, International Journal of Fatigue. 21 (1999) 889–894. https://doi.org/10.1016/S0142-1123(99)00084-5.

[49] X. Dong, H. Zhao, L. Zhang, H. Cheng, J. Gao, Geometry Effects in Four-Point Bending Test for Thin Sheet Studied by Finite Element Simulation, Mater. Trans. 57 (2016) 335–343. https://doi.org/10.2320/matertrans.M2015178.

[50] T. Lube, M. Manner, R. Danzer, The Miniaturisation of the 4-Point-Bend Test, Fatigue & Fracture of Engineering Materials & Structures. 20 (1997) 1605–1616. https://doi.org/10.1111/j.1460-2695.1997.tb01514.x.

[51] B. Bergman, On the estimation of the Weibull modulus, J Mater Sci Lett. 3 (1984) 689–692. https://doi.org/10.1007/BF00719924.

[52] J.A. Griggs, Y. Zhang, Determining the confidence intervals of Weibull parameters estimated using a more precise probability estimator, Journal of Materials Science Letters. 22 (2003) 1771–1773. https://doi.org/10.1023/B:JMSL.0000005417.39465.35.

[53] L. Song, D. Wu, Y. Li, Optimal probability estimators for determining Weibull parameters, Journal of Materials Science Letters. 22 (2003) 1651–1653. https://doi.org/10.1023/B:JMSL.0000004640.71595.f3.

[54] I.J. Davies, Unbiased estimation of Weibull modulus using linear least squares analysis—A systematic approach, Journal of the European Ceramic Society. 37 (2017) 369–380. https://doi.org/10.1016/j.jeurceramsoc.2016.07.008.

[55] S. Lee, J.-H. Kim, Y.S. Kim, T. Ohba, T.-S. Kim, Effects of Thickness and Crystallographic Orientation on Tensile Properties of Thinned Silicon Wafers, IEEE Transactions on Components, Packaging and Manufacturing Technology. 10 (2020) 296–303. https://doi.org/10.1109/TCPMT.2019.2931640.